Scientific Research Publishing

Advances in Materials Physics and Chemistry, 2022, 12, 289-305
https://www.scirp.org/journal/ampc
ISSN Online: 2162-5328
ISSN Print: 2162-531X

Local Tuning of the Surface Potential in Silicon Carriers by Ion Beam Induced Intrinsic Defects

Daniel Blaschke[1,2], Lars Rebohle[2], Ilona Skorupa[2], Heidemarie Schmidt[1,3]

[1]Leibniz Institute of Photonic Technology, Jena, Germany
[2]Helmholtz-Zentrum Dresden-Rossendorf, Institute of Ion Beam Physics and Materials Research, Dresden, Germany
[3]Friedrich Schiller University Jena, Institute for Solid State Physics, Jena, Germany
Email: daniel.blaschke@leibniz-ipht.de, heidemarie.schmidt@uni-jena.de

How to cite this paper: Blaschke, D., Rebohle, L., Skorupa, I. and Schmidt, H. (2022) Local Tuning of the Surface Potential in Silicon Carriers by Ion Beam Induced Intrinsic Defects. *Advances in Materials Physics and Chemistry*, **12**, 289-305.
https://doi.org/10.4236/ampc.2022.1211019

Received: September 21, 2022
Accepted: November 22, 2022
Published: November 25, 2022

Abstract

The immobilization of biomaterials on a carrier is the first step for many different applications in life science and medicine. The usage of surface-near electrostatic forces is one possible approach to guide the charged biomaterials to a specific location on the carrier. In this study, we investigate the effect of intrinsic defects on the surface potential of silicon carriers in the dark and under illumination by means of Kelvin probe force microscopy. The intrinsic defects were introduced into the carrier by local, stripe-patterned ion implantation of silicon ions with a fluence of 3×10^{13} Si ions/cm^2 and 3×10^{15} Si ions/cm^2 into a p-type silicon wafer with a dopant concentration of 9×10^{15} B/cm^3. The patterned implantation allows a direct comparison between the surface potential of the silicon host against the surface potential of implanted stripes. The depth of the implanted silicon ions in the target and the concentration of displaced silicon atoms was simulated using the Stopping and Range of Ions in Matter (SRIM) software. The low fluence implantation shows a negligible effect on the measured Kelvin bias in the dark, whereas the large fluence implantation leads to an increased Kelvin bias, *i.e.* to a smaller surface work function according to the contact potential difference model. Illumination causes a reduced surface band bending and surface potential in the non-implanted regions. The change of the Kelvin bias in the implanted regions under illumination provides insight into the mobility and lifetime of photo-generated electron-hole pairs. Finally, the effect of annealing on the intrinsic defect density is discussed and compared with atomic force microscopy measurements on the 2nd harmonic. In addition, by using the Baumgart, Helm, Schmidt interpretation of the measured Kelvin bias, the dopant concentration after implantation is estimated.

Keywords

Kelvin Probe Force Microscopy, Surface Potential, Intrinsic Defects, Silicon, Ion Implantation

1. Introduction

The coating of surfaces with biomaterials is an important step for many different applications, e.g. the immobilization of biomaterials on biosensors [1], the peptide immobilization on dental implants to prevent peri-implantitis [2], or the cell growth on scaffolds for tissue engineering [3] [4]. Many factors are relevant for the cell substrate interactions, e.g. substrate surface energy, surface electrostatic properties, macro- and micro-surface morphology, surface heterogeneity, functional groups, the mobility of functional groups on the surface [5]. Even by considering only the electrostatic properties of a surface, the attachment of microorganisms at a surface is a complex procedure. The charge of a microorganism or a substrate surface depends on the pH value of the surrounding medium. At the isoelectric point, no net charge exists. Above and below the isoelectric point, a net negative and positive charge is present, respectively. Many publications report on the isoelectric point, e.g. of oxides and hydroxides [6], red blood cells [7], and bacteria [8]. It is obvious that the cell surfaces of most microorganisms are negatively charged under normal pH conditions due to a prevalence of negatively charged phosphate, carboxylate, and sulfate groups in the cell wall [9]. During the first phase of static in vitro cell adhesion to a substrate, the electrostatic interaction plays an important role followed by two more phases including the flattening and spreading of the cell body and the organization of the actin skeleton with the formation of focal adhesion between the cell and the substrate [10] [11].

As we have reported in our previous work [12], these electrostatic forces can be used for the self-organized local immobilization of charged biomolecules. We controlled the surface charge pattern by a local implantation of phosphorus and boron ions into p- and n-type silicon wafers, respectively. The doping of silicon by ion implantation with group III or V elements is a standard process step in semiconductor technologies. In contrast to pH dependent charges on the substrate surface, the trapped charges at the SiO_2/Si interface, which are influenced by ion implantation, have the advantage that they are, in the first order, independent of the pH value of the surrounding medium. Hence, by choosing convenient ion implantation parameters, attractive electrostatic forces can be generated to guide the adhesion of biomaterials on the substrate, independent of the surrounding medium pH value.

In this work, we show that intrinsic defects of silicon can be electrically active and can be used to tune the surface potential locally. The intrinsic defects were introduced by a local stripe-patterned implantation of silicon ions into the sili-

con host wafer. The change in surface potential was investigated by means of Kelvin probe force microscopy (KPFM) before and after sample annealing as well as under illumination and in the dark. Defects can also be generated in other host materials, e.g. paramagnetic defects in Ga ion implanted perovskites [13].

2. Material and Methods

2.1. Sample Preparation

Intrinsic defects in silicon were introduced by ion beam implantation of silicon ions into p-doped 4 inch <100>-Si wafers with a specific resistivity of 1 - 5 Ωcm. The specific resistivity of the non-implanted wafers corresponds to a dopant concentration of $(3 - 15) \times 10^{15}$ B/cm^3. Prior to ion implantation, the wafers were RCA cleaned and a 1 µm thick SiO_2 layer was formed on top of the wafer by wet thermal oxidation to smear out the profile of the implanted silicon ions. In order to compare the surface potential of implanted and non-implanted silicon, a photolithographic step was used to prepare a stripe-patterned resist mask with 2 µm wide stripes without resist pitched by 10 µm wide stripes with resist. During the implantation, the silicon ions were stopped in the SiO_2 layer at locations covered with resist, but can penetrate into the silicon at locations without resist. After ion implantation with two different fluences, the resist mask and the SiO_2 layer were removed by a treatment in aceton and HF, respectively. Before removing the oxide layer, the samples were partially annealed in a nitrogen environment for 30 min at 900˚C.

2.2. Ion Implantation and Simulation

The simulation of the ion range and the displacement of silicon target atoms was performed using SRIM-2013.00 in the "Detailed Calculation with full Damage Cascades" mode. The energy of the implanted silicon ions was set to 970 keV to obtain a similar depth profile as by the implantation of 1 MeV phosphorus ions, which we used in our previous publication [12]. The angle of incidence was set to 7˚ tilt and 22˚ twist during ion implantation to prevent ion channeling.

2.3. AFM/KPFM Measurements

Surface potentials were characterized by KPFM measurements using the atomic force microscope (AFM) Level-AFM from Anfatec, operated under dark conditions in nitrogen atmosphere. During KPFM measurements, topography and electrical signals were probed simultaneously in amplitude modulation mode using Pt coated n-type Si cantilevers (MikroMasch HQ:NSC18/Pt, f_{res} = 75 kHz, k = 2.8 N/m) with a typical tip radius of less than 30 nm. The topography was measured at the 1st harmonic of the 1st eigenmode of the cantilever, and Kelvin bias and free charge carrier concentration were detected at the 1st and 2nd harmonic of the 2nd eigenmode, respectively. The excitation voltage U_{ac} was set to 1 V. Before starting the KPFM measurements, the contribution from the interaction between cantilever and sample surface to the electrical signal was characte-

rized by retracting the tip to a distance of 1 - 3 µm with switched off Kelvin feedback. The remaining electrical signal was used as compensation offset in the measurement software. This approach is explained in detail in Ref. [14] and allows quantitative measurements. In order to prevent the photo-generation of charge carriers during measurements in the dark, the deflection of the AFM tip was detected with an IR laser with a wavelength of 1500 nm. In addition, a green LED inside the AFM head was used to characterize the influence of photo-generated charge carriers to the KPFM signal under illumination.

3. Results and Discussion

Figure 1(a) shows the simulated trajectories of 100 silicon ions penetrating a 1 µm SiO_2/Si target. The incoming silicon ions are scattered at the lattice atoms leading to a change in direction and a loss of energy until they stop. If the energy transfer by the collision between ion and lattice atom is large enough to overcome the lattice binding energy, the lattice atom will leave its position. An easy defect type which can be produced by this process is the Frenkel pair, consisting of a vacancy and an interstitial atom. The stopping of ions in matter is a statistical process so that stopped ions will end up at different positions.

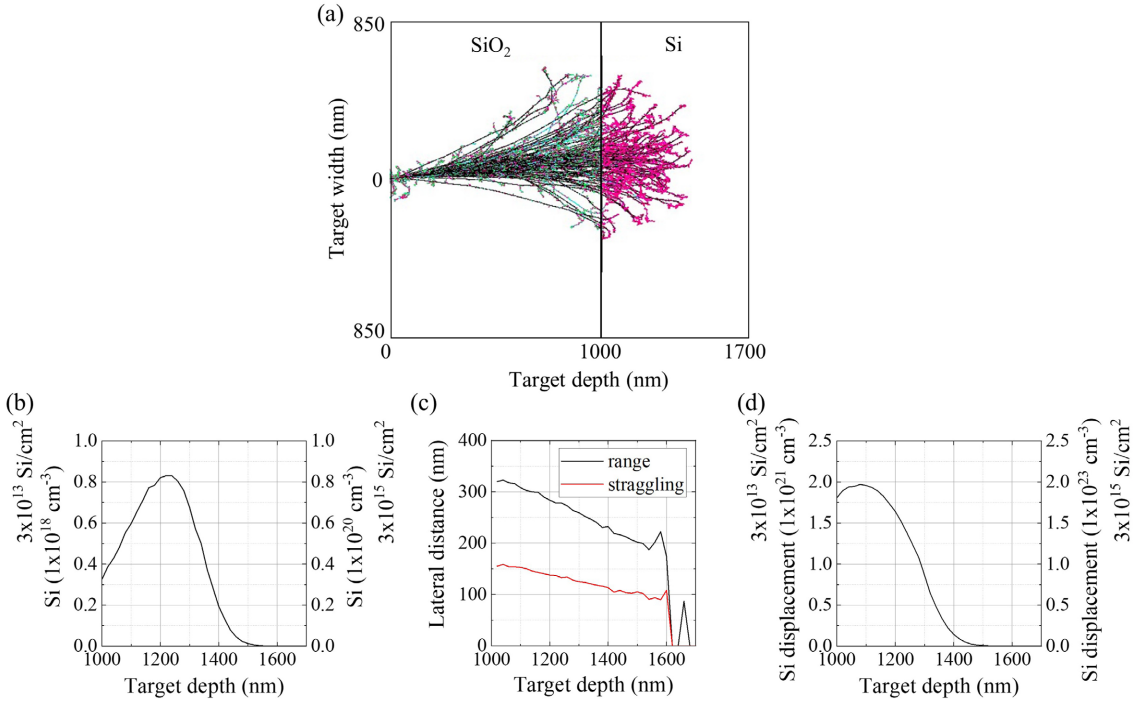

Figure 1. (a) 2D plot of a SRIM simulation of 100 silicon ions penetrating a 1 µm SiO_2/Si target using the "Detailed Calculation with full Damage Cascades" mode. The angle of incidence was set to 7˚ and the ion energy to 970 keV. The black trajectories show the path of the incoming silicon ions. Cyan and green represent moving and stopped oxygen atoms, pink and red represent moving and stopped silicon atoms from the silicon host wafer after they left their lattice position due to a collision with the incoming silicon ions, respectively. (b) Depth profile of the implanted silicon ions in the silicon target in a target depth between 1000 and 1700 nm. The left axis represent a fluence of 3×10^{13} Si/cm^2 and the right axis a fluence of 3×10^{15} Si/cm^2. (c) Lateral range and straggling of implanted silicon ions in dependence on the silicon target depths. (d) Displacement of silicon atoms of the silicon host crystal due to collisions during the ion implantation. For statistics of good quality, 99999 ions were simulated in (b)-(d).

The simulated depth profile of the implanted silicon ions, *i.e.* the location where the implanted silicon ions are stopped in a 1 µm SiO_2/Si target, is shown in **Figure 1(b)**. The profile shows the highest ion concentration in a depth of about 1230 nm and a maximum penetration depth of about 1500 nm. Due to the coverage of the silicon wafer with a 1 µm thick oxide layer during implantation, the concentration of implanted silicon atoms at the surface of the silicon wafer after removal of the oxide is far away from zero, namely 3.25×10^{17} Si/cm^3 and 3.25×10^{19} Si/cm^3 for an ion fluence of 3×10^{13} Si ions/cm^2 or 3×10^{15} Si ions/cm^2, respectively.

In addition to the ion penetration into the depth of the target, the scattering leads to a broadening into the lateral direction, see **Figure 1(c)**. Shown is the lateral distribution of the incoming silicon ions in dependence on the depth of the silicon layer with an depth averaged value of 280 nm and a straggling of about 140 nm. The straggling is defined as the square root of the variance [15]. The scattering into the lateral direction leads to a broadening of the implanted regions below the resist mask.

Figure 1(d) represents the depth profile of displaced silicon atoms of the silicon host crystal. In comparison to the maximum concentration of implanted silicon ions in **Figure 1(b)**, the highest concentration of displaced silicon atoms is shifted towards the surface of the silicon wafer with a maximal concentration in a depth of 1080 nm of about 2×10^{21} Si/cm^3 and 2×10^{23} Si/cm^3 for an ion fluence of 3×10^{13} Si ions/cm^2 and 3×10^{15} Si ions/cm^2, respectively. The atomic density of silicon is 5×10^{22} Si/cm^3 which means that for the small fluence of 3×10^{13} Si ions/cm^2, about 4% of the atoms in the silicon host crystal are displaced by the incoming ions and we can conclude that the top layer of the silicon wafer is amorphized by using the large fluence. Note that SRIM does not consider effects like defect annealing, ion channeling, fluence rate effects, and diffusion of implanted ions. Therefore, the simulated defect concentration, e.g. the concentration of displaced silicon atoms in the silicon host crystal is overestimated, **Figure 1(d)**.

Figure 2(a) shows AFM data of the 2nd harmonic of the 2nd eigenmode with switched off Kelvin feedback, *i.e.* $U_{dc} = 0$. The signal variation over implanted stripes and non-implanted silicon host crystal can be related with a variation in $\partial C/\partial z$ (see **Appendix**), which gives an information about the amount of free charge carriers which can follow the applied test voltage with amplitude U_{ac} and frequency *f*. The brighter the image, the larger $\partial C/\partial z$ and the carrier concentration. The left column of **Figure 2(a)** shows samples implanted with a fluence of 3×10^{13} Si ions/cm^2 whereas the samples shown in the right column were implanted with a fluence of 3×10^{15} Si ions/cm^2. The black arrows indicate the position of the implanted, nominal 2 µm wide, stripes running in an angle of 45˚ through the image.

For the low fluence implanted sample without annealing (**Figure 2(a)** (i)) an increased amount of free charge carriers is only visible at the edges of the ion

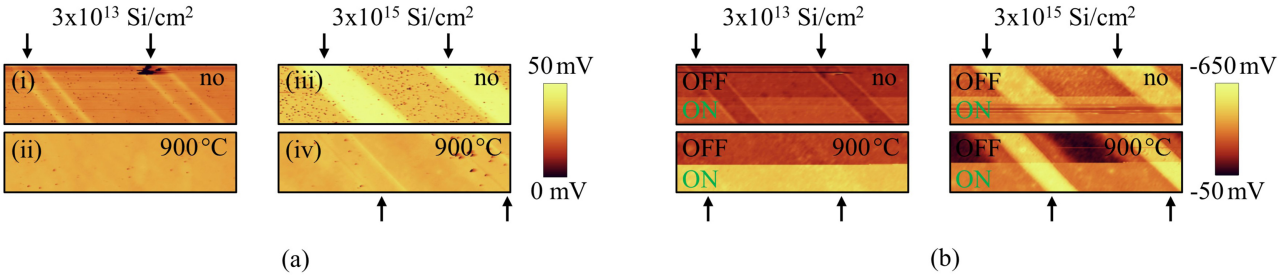

Figure 2. (a) 30.0 × 7.5 μm² large AFM images measured at the 2nd harmonic of the 2nd eigenmode of the cantilever with switched off Kelvin feedback in the dark. This signal is related with $\partial C/\partial z$ (Equation (A22) in Appendix). The arrows indicate implanted stripe-like regions with a nominal width of 2 μm and a periodicity of 12 μm. The fast scan axis had an angle of 45˚ with respect to the implanted stripes. (b) 30.0 × 7.5 μm² large KPFM images of p-doped <100>-Si samples implanted with silicon ions in a stripe-like pattern. The top of each image shows the KPFM signal under dark conditions (OFF) and the lower part shows the KPFM signal under illumination with a green LED (ON).

implanted regions. One possible explanation therefore might be the occurrence of electrically active defects due to lattice strain effects at the implanted/non-implanted border. However, the increased free charge carrier concentration vanishes after an annealing step in nitrogen atmosphere for 30 min at 900˚C, **Figure 2(a)** (ii).

In contrast, the silicon implantation with a 100 times larger fluence of 3×10^{15} Si ions/cm² results in an increased free charge carrier concentration inside the implanted stripe due to the generation of electrically active defects, **Figure 2(a)** (iii). The temperature treatment results again in a decrease of the free charge carrier concentration, but for the large fluency not all intrinsic defects could be annealed so that a slightly higher charge carrier concentration in comparison to the host material is still present, **Figure 2(a)** (iv).

Figure 2(b) shows the Kelvin bias on all four investigated samples, implanted with a fluence of 3×10^{13} Si ions/cm² on the left column and 3×10^{15} Si ions/cm² on the right column. The upper half of each image was measured under dark conditions (OFF) and the lower half of each image was measured during illumination with a green LED (ON). Note that the measurements of the Kelvin bias were performed on the same locations as the measurements on the 2nd harmonic, shown in **Figure 2(a)**, for the determination of the charge carrier density. The implanted stripes, marked with an arrow in **Figure 2(b)**, are clearly visible except for the annealed low fluence sample.

Ion implantation with the large fluence leads to an increased Kelvin bias in the implanted regions. In contrast to this, the low fluence leads only to thin bright stripes at the edges of the implanted region, possibly due to lattice strain effects. Furthermore, we could observe an increase in the Kelvin bias in the non-implanted silicon host material during illumination, which is related with the formation of photo-generated electron-hole pairs.

For a quantitative comparison of Kelvin bias variation in dependence on implantation, annealing, and illumination, we show line scans of the Kelvin bias in **Figure 3**. Note that in this case the Kelvin bias with and without illumination

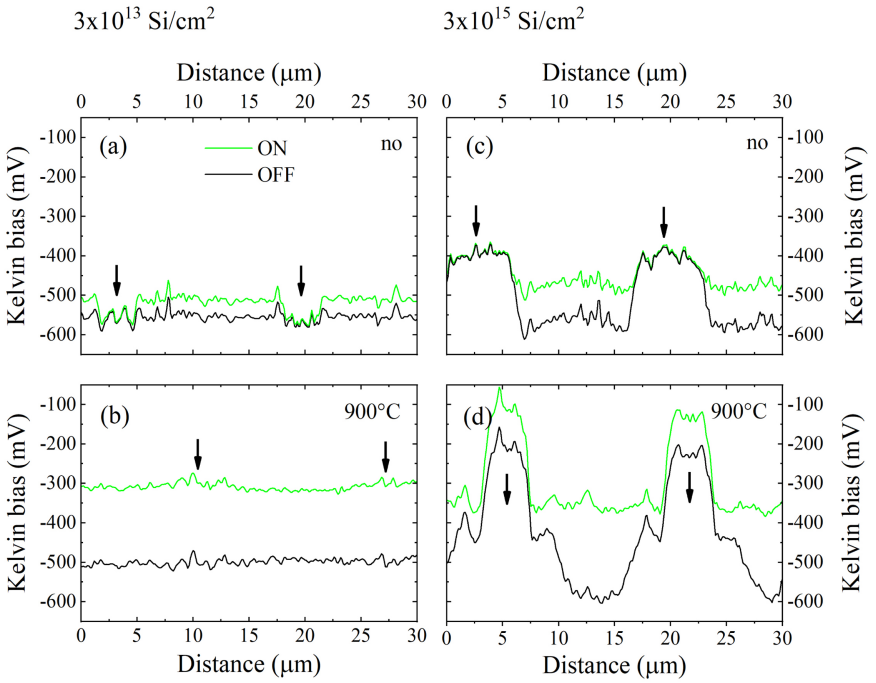

Figure 3. 30 µm line scans of KPFM measurements on p-doped <100>-Si samples, implanted with silicon ions in a stripe-like pattern with a nominal width of 2 µm pitched by 10 µm wide stripes without implantation. The line scans were performed in the dark (black) and under illumination (green) at the same position of the sample. The arrows indicate the center of the implanted stripes.

was measured by scanning a line in the dark followed by scanning the same line with illumination. This way we keep the position of implanted stripes unchanged.

The low fluence ion implantation without annealing in **Figure 3(a)** shows no significant change in the Kelvin bias during the measurement in dark (black line). One reason might be that the defect concentration is very low after implantation and the position of the Fermi level is still determined by the boron doping of the silicon host material. The number of displaced silicon atoms of the host crystal, determined with an SRIM simulation, is shown in **Figure 1(d)** which amounts to about 4% of the atoms in the silicon crystal. However, SRIM typically overestimates the defect concentration by neglecting effects like defect annealing. In addition, most of the silicon defects might be electrically not active so that they have no influence on the Fermi level. Illumination with a green LED leads to an increased Kelvin bias of about 50 mV in the non-implanted regions (green line in **Figure 3(a)**) due to the surface photovoltaic effect [16] [17] [18]. A sketch of the band diagram for p-type silicon with and without illumination is shown in Ref. [18]. Due to the downward bended bands, excess holes are swept away from the surface and excess electrons are swept towards the surface. This will reduce the density of surface trapped holes and decrease the band bending under illumination, *i.e.* the surface potential is decreased [17]. Interestingly, no change of the Kelvin bias is observed in the implanted regions. One explanation

is the fact that the formation of surface photovoltage only occurs if the generation of electron-hole pairs is followed by net charge redistribution [17]. The ion beam induced defects in the silicon lattice reduce the lifetime and mobility of the photo-generated charge carriers so that the surface potential is not influenced.

Annealing of this sample for 30 min in nitrogen atmosphere at 900˚C reduces the defect concentration in the implanted regions. Therefore, the Kelvin bias during illumination is also changed in the implanted regions, **Figure 3(b)**.

In **Figure 3(c)** the Kelvin bias for an ion fluence of 3×10^{15} Si ions/cm^2 is shown. The large fluence introduces many lattice defects into the Si host crystal, see **Figure 1(d)**. At least every silicon atom was hit by an incoming ion so that we can expect an amorphization of the silicon host crystal. Therefore, the Fermi level is changed and the measured Kelvin bias is about 170 mV higher in the implanted stripes in comparison to the non-implanted regions. Note that the stripe width with an increased Kelvin bias is larger than the expected 2 µm. This is most probably caused by a too large stripe width without resist during ion implantation. In addition, during the ion penetration into the depth of the silicon, they will be also scattered in-plane. Using SRIM we simulated a value of about 0.28 µm with a straggling of 0.14 µm, **Figure 1(c)**. Therefore, we can expect that the broadening of the implanted area is in the order of 1 µm due to the ion scattering. Illumination of the sample leads to an increased Kelvin bias of about 100 mV in the non-implanted areas due to the reduced band bending as already described in **Figure 3(a)**. However, due to the small lifetime and mobility of the photo-generated charge carriers in the high defect region of the implanted stripes, no change in the Kelvin bias is observed.

Annealing of this sample (**Figure 3(d)**) increases the Kelvin bias variation between implanted and non-implanted regions by about 370 mV without illumination. Interestingly, the strong variation was only observed in the middle of the implanted stripes. At the boundaries of the implanted stripes, the Kelvin bias shows a similar value as before annealing, **Figure 3(c)**. This causes the shoulder-like feature on both sides of the KPFM signal. In addition, the width of the stripes with a changed Kelvin bias increases and the transition between implanted and non-implanted regions is smoother. The broadening of the stripes might be explained with the diffusion of defects from the disturbed implanted regions into the silicon host wafer. Furthermore, lattice strain effects by a partly recrystallization of the amorphized regions during annealing could be an additional explanation. The increased Kelvin bias in the implanted region means that annealing does not remove all ion induced defects after introducing a high amount of damage (amorphization) by using a fluence of 3×10^{15} Si ions/cm^2. In contrast, all defects influencing the Kelvin bias could be annealed, if only about 4% of the silicon atoms were displaced by using a 100 times smaller fluence of 3×10^{13} Si ions/cm^2 (**Figure 3(b)**). Illumination increases the measured Kelvin bias by about 230 mV in the non-implanted and 100 mV in the implanted regions. In contrast to the non-annealed samples in **Figure 3(a)** and **Figure 3(c)**, illumina-

tion also effects the Kelvin bias in the implanted regions. This hints towards an increased lifetime and mobility of the photo-generated charge carriers due to annealing so that the band bending at the surface is influenced by charge redistribution. However, the Kelvin bias variation with and without illumination is still smaller in the implanted region as in the non-implanted region.

The contact potential difference (CPD) model, see Appendix, can be used to explain the above observed influence of illumination by a reduction of the band bending due to the surface photovoltage effect. However, the dopant concentration in the implanted regions cannot be calculated using the CPD model, because the calculated Kelvin bias U_K^{CPD} also depends on the band bending (Equations (17)-(19)), which is most probably different for implanted and non-implanted regions as a result of different defects at the SiO_2/Si interface. The Baumgart, Helm, Schmidt (BHS) model intrinsically includes the band bending due to the interface defects, see Appendix, but in contrast to the CPD model, the amount and energetic positions of the defects play no role. Important are the bulk properties of the material *i.e.* the position of the Fermi level in the bulk. Therefore, it is possible to calculate the effective doping concentration in the implanted regions from the shift of the measured Kelvin bias in the dark. In **Figure 4** the position of the Fermi level in dependence on the doping concentration and the binding energy of donors or acceptors is shown, whereas the Fermi level of the intrinsic silicon was set to zero. We have chosen intrinsic defects with binding energies in the range from 10 meV to 300 meV due to many possible defect types after ion implantation. For a review on possible defects in silicon and their position in the bandgap we refer to Refs. [19] [20] [21]. The Fermi level of the p-doped host wafer with a doping concentration of about 9×10^{15} B/cm^3 was calculated to −354 meV, which is 183 meV above the valence band edge.

The black lines in **Figure 3** represent the line scans of the Kelvin bias in the dark. For the low fluence samples ((a), (b)), the measured Kelvin bias is similar for implanted and non-implanted regions so that we do not expect a change in the effective doping concentration.

In contrast, the Kelvin bias for the high fluence sample without annealing **Figure 3(c)** is about 170 mV larger in the implanted region as in the non-implanted one. This is fulfilled if after Equation (A15), $E_V - E_F(p) = -183\,\text{meV}$ is reduced by 170 meV to $E_V - E_F(p) = -13\,\text{meV}$ for the non-implanted and implanted region, respectively. By assuming some uncertainties in the doping level of the host wafer and during KPFM measurements, one can conclude that the Fermi lies near one of the two band edges. This implies a doping concentration after ion implantation which amounts to 1×10^{20} cm^{-3} or even higher in dependence on the defect binding energy (**Figure 4**). The large doping concentration is confirmed by the bright stripes in the measurements of the 2nd harmonic in **Figure 2(a)** (iii). In agreement with the BHS model, the Fermi level lies nearby the band edge for n- or p-type material, but it is not possible to conclude which defect type dominates after ion implantation without annealing. If donors dominate,

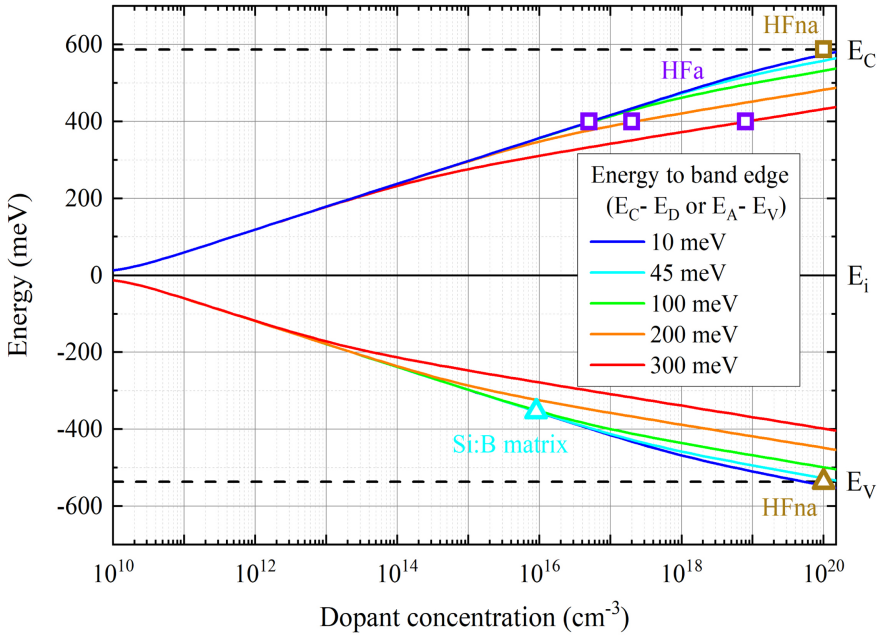

Figure 4. Calculated Fermi level of different defect states in silicon in dependence on the dopant concentration and dopant ionization energy at 300 K. The intrinsic Fermi level E_i was set to zero. The positions of the conduction band edge E_C and valence band edge E_V are illustrated by the dashed black lines. It is assumed that E_C and E_V do not depend on the dopant concentration. The cyan triangle represents the dopant concentration of the p-doped silicon host wafer (Si:B matrix) from the data sheet. The brown triangle represents the dopant concentration after implantation in the high fluence sample without annealing (HFna) in the case of p-type conductivity (intrinsic acceptors). The brown square represents the dopant concentration for the HFna sample in the case of n-type conductivity (intrinsic donors). The violet squares show possible dopant concentrations for the high fluence sample with annealing (HFa) in dependence on different ionization energies of the donors.

the Fermi level would lie close to the conduction band edge, see HFna labeled square in **Figure 4**. If acceptors dominate, the Fermi level would lie close to the valence band edge (HFna labeled triangle in **Figure 4**).

Annealing of this sample increases the measured Kelvin bias by about 370 mV in the center of the implanted stripes whereas the shoulders show a similar increase as in the non-annealed case, see **Figure 3(d)**. The increase of 370 mV means that the doping type is changed from p in the host wafer to n in the center of the implanted stripes. The energy difference between the conduction band and the Fermi level in the n-type region has to be 370 meV - 183 meV = 187 meV. In dependence on the binding energy of possible defects, a doping concentration of 5×10^{16} cm^{-3}, 2×10^{17} cm^{-3}, or 8×10^{18} cm^{-3} is expected for the cases calculated in **Figure 4** with a binding energy of less or similar than 100 meV, 200 meV, or 300 meV, respectively. Most probably, not only one defect type is present after ion implantation and annealing. The observed and modeled reduction of the effective doping concentration after annealing is confirmed by a comparison of the measurements on the 2nd harmonic in **Figure 2(a)** ((iii), (iv)).

4. Conclusions

Intrinsic defects were introduced in silicon by a local, stripe-patterned implantation of silicon ions into a p-type silicon host wafer with an energy of 970 keV and a fluence of 3×10^{13} Si ions/cm^2 and 3×10^{15} Si ions/cm^2. The p-type silicon host wafer was covered with a 1 µm thick SiO_2 layer to broaden the implantation profile. After the implantation of silicon ions and partially sample annealing, the SiO_2 layer was removed to investigate the effect of intrinsic defects on the silicon surface potential by means of Kelvin probe force microscopy. The maximum penetration depths of the silicon ions into the p-type silicon host wafer were simulated using SRIM to be about 500 nm, and the number of displaced silicon atoms from the host lattice by collisions with the incoming ions was about 4% for the small fluence sample, leading to amorphization by using the large fluence.

Before annealing the small fluence sample reveals an increased free charge carrier density and a slightly increased Kelvin bias at the border between implanted and non-implanated stripes. After annealing at 900˚C in nitrogen atmosphere for 30 min the increased free charge carrier concentration has vanished. Increased carrier lifetime and mobility in small fluence sample after annealing is confirmed by the Kelvin bias measurement under illumination.

In contrast, before annealing the large fluence sample showed a strongly increased free charge carrier concentration and Kelvin bias in the whole implanted stripe. An effective dopant concentration of at least 1×10^{20} cm^{-3} has been derived by the BHS model. After annealing the large fluence sample reveals n-type conductivity and a strongly reduced effective dopant concentration of about 5×10^{16} cm^{-3}.

In conclusion, if the intrinsic defect concentration in silicon is small, a subsequent thermal treatment completely anneals intrinsic defects which are able to influence the Kelvin bias signal. Large concentrations of intrinsic defects are reduced but not completely eliminated by the thermal treatment.

Acknowledgements

The authors thank S. Hartmann for initiating the silicon implantation into silicon wafers for KPFM measurements as a comparison to boron and phosphorus implantation into silicon wafers. Furthermore, financial support is from the Sächsische Aufbaubank (SAB-Project 100260515), Thüringer Aufbaubank (EFRE-OP 2014-2020), as well as the support by the Ion Beam Center (IBC) at HZDR, is gratefully acknowledged.

Conflicts of Interest

The authors declare no conflicts of interest regarding the publication of this paper.

References

[1] D'Souza, S.F. (2001) Immobilization and Stabilization of Biomaterials for Biosensor

Applications. *Applied Biochemistry and Biotechnology*, **96**, 225-238. https://doi.org/10.1385/ABAB:96:1-3:225

[2] Fischer, N.G., Jiahe, H. and Conrado, A. (2020) Surface Immobilization Chemistry of a Laminin-Derived Peptide Affects Keratinocyte Activity. *Coatings*, **10**, Article No. 560. https://doi.org/10.3390/coatings10060560

[3] Majhy, B., Priyadarshini, P. and Sen, A.K. (2021) Effect of Surface Energy and Roughness on Cell Adhesion and Growth-Facile Surface Modification for Enhanced Cell Culture. *RSC Advances*, **11**, 15467-15476. https://doi.org/10.1039/D1RA02402G

[4] O'Brien, F.J. (2011) Biomaterials & Scaffolds for Tissue Engineering. *Materials Today*, **14**, 88-95. https://doi.org/10.1016/S1369-7021(11)70058-X

[5] Arima, Y. and Iwata, H. (2015) Preferential Adsorption of Cell Adhesive Proteins from Complex Media on Self-Assembled Monolayers and Its Effect on Subsequent Cell Adhesion. *Acta Biomaterialia*, **26**, 72-81. https://doi.org/10.1016/j.actbio.2015.08.033

[6] Yoon, R.H., Salman, T. and Donnay, G. (1979) Predicting Points of Zero Charge of Oxides and Hydroxides. *Journal of Colloid and Interface Science*, **70**, 483-493. https://doi.org/10.1016/0021-9797(79)90056-0

[7] Coulter, C.B. (1921) The Isoelectric Point of Red Blood Cells and Its Relation to Agglutination. *Journal of General Physiology*, **3**, 309-323. https://doi.org/10.1085/jgp.3.3.309

[8] Harden, V.P. and Harris, J.O. (1953) The Isoelectric Point of Bacterial Cells. *Journal of Bacteriology*, **65**, 198-202. https://doi.org/10.1128/jb.65.2.198-202.1953

[9] Škvarla, J. (1993) A Physico-Chemical Model of Microbial Adhesion. *Journal of the Chemical Society, Faraday Transactions*, **89**, 2913-2921. https://doi.org/10.1039/FT9938902913

[10] Metwally, S. and Stachewicz, U. (2019) Surface Potential and Charges Impact on Cell Responses on Biomaterials Interfaces for Medical Applications. *Materials Science and Engineering: C*, **104**, Article ID: 109883. https://doi.org/10.1016/j.msec.2019.109883

[11] Khalili, A.A. and Ahmad, M.R. (2015) A Review of Cell Adhesion Studies for Biomedical and Biological Applications. *International Journal of Molecular Sciences*, **16**, 18149-18184. https://doi.org/10.3390/ijms160818149

[12] Blaschke, D., Pahlow, S., Fremberg, T., Weber, K., Müller, A.D., Kurz, S., Spohn, J., Dhandapani, V., Rebohle, L., Skorupa, I. and Schmidt, H. (2021) Functionalized Silicon Substrates with Stripe-Patterned Surface-Near Electrostatic Forces for the Self-Organized, Stable Immobilization of Biomolecules. *Applied Surface Science*, **545**, Article ID: 148729. https://doi.org/10.1016/j.apsusc.2020.148729

[13] Jeon, N.J., Seo, J., Kim, Y., Lee, J.Y., Hong, S., Kim, S.H. and Lee, J.-K. (2022) Focused-Ion-Beam Induced Paramagnetic Defects in FAMn:PbI3 Perovskite Films. *Advances in Chemical Engineering and Science*, **12**, 87-95. https://doi.org/10.4236/aces.2022.122007

[14] Müller, F. and Müller, A.D. (2009) Frequency Dependent Kelvin Probe Force Microscopy on Silicon Surfaces. *Journal of Vacuum Science & Technology B: Microelectronics and Nanometer Structures Processing, Measurement, and Phenomena*, **27**, 969-974. https://doi.org/10.1116/1.3039682

[15] Ziegler, J.F., Biersack, J.P. and Ziegler, M.D. (2008) TRIM—Setup and Input. *SRIM—The Stopping and Range of Ions in Matter*. SRIM Company, 8-26.

http://www.srim.org/SRIM/SRIM%2008.pdf

[16] Kronik, L. and Shapira, Y. (1999) Surface Photovoltage Phenomena: Theory, Experiment, and Applications. *Surface Science Reports*, **37**, 1-206. https://doi.org/10.1016/S0167-5729(99)00002-3

[17] Kronik, L. and Shapira, Y. (2001) Surface Photovoltage Spectroscopy of Semiconductor Structures: At the Crossroads of Physics, Chemistry and Electrical Engineering. *Surface and Interface Analysis*, **31**, 954-965. https://doi.org/10.1002/sia.1132

[18] Votoček, L. and Toušek, J. (2005) Surface Photovoltaic Effect and Its Applications to Si Wafers and Monocrystalline Si Solar Cells Diagnostics. *Proceedings of the* 14*th Annual Conference of Doctoral Students—WDS* 2005, Prague, 7-10 June 2005, 595-600.

[19] Watkins, G.D. (2000) Intrinsic Defects in Silicon. *Materials Science in Semiconductor Processing*, **3**, 227-235.

[20] Watkins, G.D. (2013) Intrinsic Point Defects in Semiconductors 1999. In: Cahn, R.W., Haasen, P. and Kramer, E.J., Eds., *Materials Science and Technology*, Wiley, Hoboken. https://doi.org/10.1002/9783527603978.mst0244

[21] Pichler, P. (2004) Intrinsic Point Defects. In: *Intrinsic Point Defects*, *Impurities*, *and Their Diffusion in Silicon*, Springer, Vienna. https://doi.org/10.1007/978-3-7091-0597-9_2

[22] Grundmann, M. (2006) The Physics of Semiconductors: An Introduction Including Devices and Nanophysics. Springer, Berlin.

[23] Sze, S.M. and Ng, K.K. (2006) Physics and Properties of Semiconductors—A Review. In: Sze, S. and Ng, K.K., Eds., *Physics of Semiconductor Devices*, John Wiley & Sons, Hoboken. https://doi.org/10.1002/9780470068328.ch1

[24] Baumgart, C., Helm, M. and Schmidt, H. (2009) Quantitative Dopant Profiling in Semiconductors: A Kelvin Probe Force Microscopy Model. *Physical Review B*, **80**, Article ID: 085305. https://doi.org/10.1103/PhysRevB.80.085305

[25] Nonnenmacher, M., O'Boyle, M.P. and Wickramasinghe, H.K. (1991) Kelvin Probe Force Microscopy. *Applied Physics Letters*, **58**, 2921-2923. https://doi.org/10.1063/1.105227

[26] Henning, A.K., Hochwitz, T., Slinkman, J., Never, J., Hoffmann, S., Kaszuba, P. and Daghlian, C. (1995) Two-Dimensional Surface Dopant Profiling in Silicon Using Scanning Kelvin Probe Microscopy. *Journal of Applied Physics*, **77**, 1888-1896. https://doi.org/10.1063/1.358819

[27] Polak, L. and Wijngaarden, R.J. (2016) Two Competing Interpretations of Kelvin Probe Force Microscopy on Semiconductors Put to Test. *Physical Review B*, **93**, Article ID: 195320. https://doi.org/10.1103/PhysRevB.93.195320

[28] Axt, A., Hermes, I.M., Bergmann, V.W., Tausendpfund, N. and Weber, S.A.L. (2018) Know Your Full Potential: Quantitative Kelvin Probe Force Microscopy on Nanoscale Electrical Devices. *Beilstein Journal of Nanotechnology*, **9**, 1809-1819. https://doi.org/10.3762/bjnano.9.172

Appendix

1.1. Calculation of Fermi Energy

The determination of the Fermi energy is discussed in detail in Refs. [22] [23]. Here, we will shortly summarize the equations which were used to calculate the Fermi energy values in **Figure 4**. If it is not declared otherwise, the equations and given values are taken from Ref. [22].

For the calculation of the Fermi energy position, the charge neutrality condition has to be solved,

$$-n + p - N_A^- + N_D^+ = 0, \tag{A1}$$

where N_D^+ and N_A^- is the concentration of the ionized donors and acceptors, respectively. The density of electrons n in the conduction band is given by

$$n = \int_{E_C}^{\infty} D_e(E)\, f_e(E)\, \mathrm{d}E, \tag{A2}$$

and the density of holes p in the valence band is given by

$$p = \int_{-\infty}^{E_V} D_h(E)\, f_h(E)\, \mathrm{d}E, \tag{A3}$$

where $D_e(E)$ and $D_h(E)$ is the density of states in the conduction band and valence band, respectively.

In thermodynamic equilibrium, the Fermi-Dirac distribution for electrons $f_e(E)$ or for holes $f_h(E)$ describes the probability that an electronic state is occupied at temperature T:

$$f_e(E) = \frac{1}{\exp\left(\dfrac{E - E_F}{kT}\right) + 1} \tag{A4}$$

$$f_h(E) = \frac{1}{\exp\left(-\dfrac{E - E_F}{kT}\right) + 1} \tag{A5}$$

The integral in Equations (A2) and (A3) cannot be solved analytically. Therefore, the Fermi integral is used, which is defined as:

$$F_n(x) = \frac{2}{\sqrt{\pi}} \int_0^{\infty} \frac{y^n}{1 + \exp(y - x)} \mathrm{d}y \tag{A6}$$

with $n = 1/2$ for bulk materials.

The free carrier densities are then expressed by:

$$n = N_C F_{1/2}\left(\frac{E_F - E_C}{kT}\right), \tag{A7}$$

$$p = N_V F_{1/2}\left(-\frac{E_F - E_V}{kT}\right), \tag{A8}$$

where N_C and N_V describes the conduction band edge density and valence band edge density, respectively.

The ionized concentration of donors N_D^+ is given by:

$$N_D^+ = \frac{N_D}{1+\hat{g}_D \exp\left(\frac{E_F - E_D}{kT}\right)}, \tag{A9}$$

and of acceptors N_A^-

$$N_A^- = \frac{N_A}{1+\hat{g}_A \exp\left(-\frac{E_F - E_A}{kT}\right)}. \tag{A10}$$

$E_C - E_D$ and $E_A - E_V$ are the donor and acceptor binding energies, respectively (**Figure 4**). The ground-state degeneracy of the donor impurity $\hat{g}_D$ and the acceptor impurity $\hat{g}_A$ is 2 and 4, respectively [23]. In the absence of acceptors, the charge neutrality Equation (A1) simplifies to $-n + p + N_D^+ = 0$ with $p = n_i^2 / n$. Hence, the equation

$$-N_C F_{1/2}\left(\frac{E_F - E_C}{kT}\right) + \frac{n_i^2}{N_C F_{1/2}\left(\frac{E_F - E_C}{kT}\right)} + \frac{N_D}{1+\hat{g}_D \exp\left(\frac{E_F - E_D}{kT}\right)} = 0 \tag{A11}$$

has to be solved numerically. In intrinsic silicon at room temperature, the concentration of electrons is $n_i = 1\times10^{10}\ \mathrm{cm}^{-3}$. Without donors, Equation (A1) can be written as $-n + p - N_A^- = 0$ with $n = n_i^2 / p$. Hence, the equation

$$-\frac{n_i^2}{N_V F_{1/2}\left(-\frac{E_F - E_V}{kT}\right)} + N_V F_{1/2}\left(-\frac{E_F - E_V}{kT}\right) - \frac{N_A}{1+\hat{g}_A \exp\left(-\frac{E_F - E_A}{kT}\right)} = 0 \tag{A12}$$

has to be solved numerically.

The result is shown in **Figure 4** for different binding energies of donors and acceptors, where the Fermi level of the intrinsic silicon was set to zero.

The Fermi level of intrinsic silicon was calculated by:

$$E_i = \frac{E_V + E_C}{2} + \frac{kT}{2}\ln\left(\frac{N_V}{N_C}\right), \tag{A13}$$

where $N_C = 7.28\times10^{19}\ \mathrm{cm}^{-3}$ and $N_V = 1.05\times10^{19}\ \mathrm{cm}^{-3}$ at 300 K. E_C and E_V has been determined from Equation (A13) with $E_g = E_C - E_V$ and $E_g = 1.124\ \mathrm{eV}$.

1.2. Analysis of Local Kelvin Bias Variation

In literature, two main models for the interpretation of the measured Kelvin bias of semiconductors exist. One is the Baumgart, Helm, and Schmidt (BHS) model [24]. This model assumes that the electrostatic force between the AFM tip of the KPFM system and the semiconductor has its origin in the asymmetric electric dipole formed within the semiconductor surface region. In the case of silicon, this asymmetric electric dipole is formed by the charged interface states at the native silicon dioxide/doped silicon interface and the ionized dopant ions in the surface-near depletion layer. According to this model, the measured Kelvin bias is correlated with the energy difference between the respective band edge and the

Fermi level. This bias is needed during KPFM measurements to inject majority charge carriers in the surface region to neutralize charged dopants in the surface region and thus to nullify electrostatic forces which are induced by the surface potential of the asymmetric electric dipole. The analysis of Kelvin bias recorded on doped silicon relies on reference measurements on different sample positions in order to account for offsets in the Kelvin bias which can be caused by surface charges and charges trapped in the native oxide. Homogeneously distributed surface and oxide charges change the surface potential at all sample positions, *i.e.* introduce a constant offset. In the case of a n-type semiconductor:

$$eU_K^{BHS}\left(n\text{-type}\right) = E_C - E_F\left(n\right) + eU_{off}, \tag{A14}$$

and in the case of a p-type semiconductor:

$$eU_K^{BHS}\left(p\text{-type}\right) = E_V - E_F\left(p\right) + eU_{off}, \tag{A15}$$

where e is the positive elementary charge and U_{off} is an additional offset bias which depends on charges on the surface and in the oxide. Note that in the BHS model the measured Kelvin bias is independent on the probe potential. In the ideal case of no KPFM offset bias, the measured Kelvin bias is positive on n-type regions and negative on p-type regions. The absolute value of the Kelvin bias will increase with a decreasing dopant concentration.

We assume that the offset bias is the same over the whole sample, e.g. on both sides of a pn-junction. Therefore, over a pn-junction the Kelvin bias difference ΔU_K^{BHS} is expressed by:

$$e\Delta U_K^{BHS} = E_g - E_F\left(n\right) + E_F\left(p\right). \tag{A16}$$

An older model used to explain the measured Kelvin bias is the so called contact potential difference (CPD) model [25] [26] [27]. In the CPD model the measured Kelvin bias U_K^{CPD} is given by the difference between the work functions of the sample W_s and the probe W_p.

$$eU_K^{CPD} = W_s - W_p \tag{A17}$$

For a n-type semiconductor the work function is given by [27]:

$$W_s\left(n\text{-type}\right) = E_C - E_F\left(n\right) + \chi - e\phi_s - eU_s\left(n\right), \tag{A18}$$

where χ is the electron affinity, ϕ_s is a potential step at the surface of the semiconductor due to a fixed dipole layer as a result of surface termination or a molecular layer adhered to the surface, and $U_s\left(n\right)$ is the potential difference between the bulk and the surface of the semiconductor (band bending potential).

For a p-type semiconductor the work function is given by [27]:

$$W_s\left(p\text{-type}\right) = E_C - E_F\left(p\right) + \chi - e\phi_s - eU_s\left(p\right). \tag{A19}$$

Note that for a n-type semiconductor $U_s\left(n\right)$ is negative and for a p-type semiconductor $U_s\left(p\right)$ is positive. Therefore, the correction due to band bending $U_s\left(n\right)$ and $U_s\left(p\right)$ increases $W_s\left(n\text{-type}\right)$ and decreases $W_s\left(p\text{-type}\right)$.

For a pn-junction, we can assume that the fixed surface dipole layer ϕ_s is

equal on both sides. Hence, the Kelvin bias difference ΔU_K^{CPD} is given by:

$$e \cdot \Delta U_K^{CPD} = E_F(n) - E_F(p) - eU_s(p) + eU_s(n) \tag{A20}$$

Beside the measurements on the 1st harmonic, measurements on the 2nd harmonic offer the possibility to compare the dopant concentrations via its dependence on the capacitance gradient $\partial C/\partial z$. The 2nd harmonic force F_{2f} is given by [28]:

$$F_{2f} = -\frac{\partial C}{\partial z}\frac{1}{4}U_{ac}^2\left[\cos\left(2\pi 2ft\right)\right], \tag{A21}$$

where U_{ac} is the amplitude of the applied voltage with frequency *f*. In a first order approximation, the total capacitance of the probe-sample system can be considered as a serial connection of the capacitance between probe and sample surface C_i and the depletion layer capacitance inside the semiconductor next to the surface C_d. By assuming $C_i \gg C_d$, the capacitance gradient is given by:

$$\frac{\partial C}{\partial z} \propto \frac{\varepsilon_s N}{C_i^2}\frac{\partial C_i}{\partial z}, \tag{A22}$$

were N is the doping concentration of the semiconductor which equals the free carrier concentration if all dopants are ionized. This derivation is explained in more detail in [12].